

PAPER

View Article Online  
View Journal | View Issue



Cite this: *Biomater. Sci.*, 2021, **9**, 4728

# Ag functionalized SnS<sub>2</sub> with enhanced photothermal activity for safe and efficient wound disinfection†

Jun Yang,<sup>‡a</sup> Lin Sun,<sup>‡a</sup> Shuhan Hui,<sup>a</sup> Peng Zhang,<sup>a</sup> Jian Li,<sup>‡b</sup> Dong Wang,<sup>‡c</sup> Xuelin Wang,<sup>‡b</sup> and Shan Jiang,<sup>‡a</sup>

Severe bacterial infections have brought an urgent threat to our daily life, and photothermal therapy (PTT) has acted as an effective method to kill bacteria. Herein we decorated Ag on the surface of SnS<sub>2</sub> (Ag@SnS<sub>2</sub>), which has outstanding photothermal conversion capability and good biocompatibility. The decoration of Ag on SnS<sub>2</sub> improved the absorption of near-infrared (NIR) light in comparison to SnS<sub>2</sub>, resulting in a temperature increase of 50 °C after 5 min of NIR light irradiation (1.9 W cm<sup>-2</sup>) and a photothermal conversion efficiency of 31.3%. Ag@SnS<sub>2</sub> exhibits almost 100% growth inhibition of *E. coli* and *S. aureus* bacteria due to hyperthermia, with a concentration larger than 0.5 mg mL<sup>-1</sup> and 5 min of NIR irradiation. Meanwhile, SEM images of treated bacterial cells showed the attachment of Ag@SnS<sub>2</sub> on the cell surface and obvious cellular membrane destruction. Ag@SnS<sub>2</sub> can also accelerate *in vivo* wound healing through PTT-induced bacterial disinfection. Therefore, Ag@SnS<sub>2</sub> exhibits great potential for photothermal antibacterial application and wound disinfection.

Received 19th March 2021

Accepted 7th May 2021

DOI: 10.1039/d1bm00429h

rsc.li/biomaterials-science

## Introduction

Bacterial infections are one of the greatest threats to global human health.<sup>1,2</sup> It is reported that bacterial infections have about 17 billion victims every year.<sup>3</sup> The rapid growth of bacterial infections has made the study of antibacterial methods and materials urgent. Promoted by nanotechnology, versatile antibacterial strategies have been proposed for defeating bacterial infection, including chemotherapies using metal nanoparticles (e.g., silver-based antibacterial materials,<sup>4–6</sup> copper-based antibacterial materials,<sup>7</sup> and Zn-based antibacterial agents<sup>8</sup>), photodynamic therapy,<sup>9,10</sup> photothermal therapy (PTT),<sup>11,12</sup> and synergistic antibacterial therapy.<sup>13</sup>

PTT is a method inhibiting bacterial growth<sup>2,14</sup> or destroying tumor,<sup>15–18</sup> which relies on hyperthermia from photothermal agents (PTAs) when exposed to light. Particularly, near-

infrared (NIR) PTT has attracted our attention due to deep tissue penetration of NIR light and high therapeutic efficiency. Recently, various PTAs have been developed, including organic dyes and polymers,<sup>19</sup> noble metal materials,<sup>20,21</sup> carbon-based nanomaterials,<sup>22,23</sup> and semiconductor nanomaterials.<sup>24–26</sup> Among them, metal oxides and chalcogenides have been considered as one of the most attractive PTAs in recent years due to their unique features including good photothermal stability, high NIR photothermal conversion efficiency, low-cost and rapid facile synthesis.<sup>27</sup> Tin(IV) sulfide (SnS<sub>2</sub>) is a typical metal chalcogenide semiconductor with a hexagonal CdI<sub>2</sub>-type structure of the crystal and a band gap of about 2.2 eV.<sup>28–30</sup> In recent studies, SnS<sub>2</sub> has been applied in photoconductors,<sup>31</sup> solar cells,<sup>32</sup> and sensors.<sup>33</sup> Particularly, SnS<sub>2</sub> can be used as a visible-light-driven photocatalyst, because it shows a superior visible light absorption ability.<sup>34</sup> However, SnS<sub>2</sub> shows slight absorption in the NIR region, resulting in few applications in the NIR-responsive semiconductor photothermal therapy.

Most efforts have been devoted to improving the semiconductor's NIR light response, including the construction of specific morphology,<sup>35,36</sup> integration with photothermal agents,<sup>24,37</sup> and localized surface plasmon resonance (LSPR) modulation.<sup>38,39</sup> LSPR is a phenomenon where optical excitation induces cooperative oscillations of free axisymmetric electric charges limited in novel metals or semiconductor materials.<sup>40</sup> LSPR properties of semiconductor materials can be precisely modulated from the visible spectral range to the

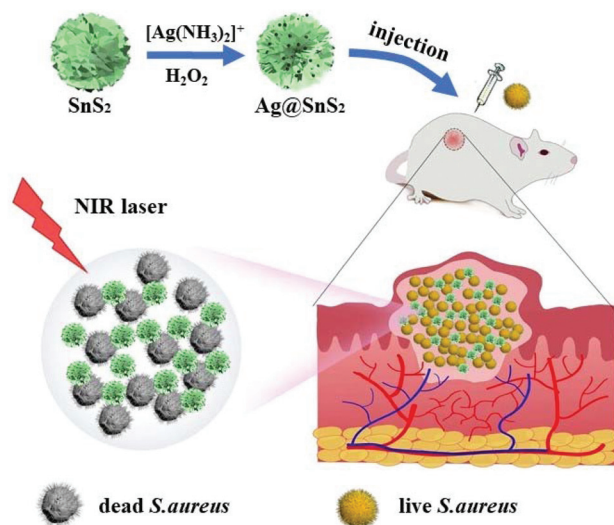
<sup>a</sup>Institute of Physical Chemistry, College of Chemistry, Jilin University, Changchun 130012, P.R. China. E-mail: sjiang@jlu.edu.cn

<sup>b</sup>Key Laboratory of Zoonosis Research, Ministry of Education, Institute of Zoonosis, College of Veterinary Medicine, Jilin University, Changchun 130062, P.R. China. E-mail: xuelin@jlu.edu.cn

<sup>c</sup>College of Chemical Engineering, Northeast Electric Power University, Jilin City 132012, P. R. China

†Electronic supplementary information (ESI) available. See DOI: 10.1039/d1bm00429h

‡These authors contributed equally to this work.



**Scheme 1** Schematic illustration of Ag@SnS<sub>2</sub> for the material synthesis and wound disinfection process.

far-infrared spectral range *via* doping or chemical post-synthesis reactions.<sup>41</sup> To maximize the LSPR in the NIR window, novel metals have been integrated into the semiconductors to form heterojunction nanostructures that have higher extinction cross-sections compared to the single-ingredient ones. The semiconductor/metal plasmonic heterostructures have exhibited promising results for photothermal therapy. For example, Cao *et al.* found that the Au@Cu<sub>2-x</sub>S heterogeneous nanomaterials had a photothermal conversion efficiency of 35.2% and an improvement of 11.3% over Cu<sub>2-x</sub>S, for the reason that the LSPR effect was formed between Au and Cu<sub>2-x</sub>S.<sup>38</sup> Similarly, Lin's group demonstrated that the CeVO<sub>4</sub>/Ag nanohybrids have improved photothermal conversion capability compared to single CeVO<sub>4</sub>, due to the LSPR property of Ag.<sup>39</sup>

Herein, plasmonic Ag was decorated on the surface of SnS<sub>2</sub> nanoflowers (Ag@SnS<sub>2</sub>) to enhance their absorption of NIR light and further improve their photothermal transduction capability. The *in vitro* bactericidal activity of Ag@SnS<sub>2</sub> was studied against Gram-negative *E. coli* and Gram-positive *S. aureus* bacteria, and the *in vivo* bactericidal activity was verified in the mice model with *S. aureus* infection (Scheme 1). Our results suggested that Ag@SnS<sub>2</sub> exhibited enhanced photothermal conversion activities and safe skin wound disinfection effects.

## Experimental

### Materials and chemicals

Stannic chloride (SnCl<sub>4</sub>·5H<sub>2</sub>O) was obtained from Aladdin Reagent (Shanghai, China). L-Cysteine was obtained from Sigma Aldrich. Silver nitrate and hydrogen peroxide were obtained from Sinopharm Chemical Reagent. Luria-Bertani (LB) broth medium and LB nutrient agar were obtained from

Qingdao Haibo Biotechnology. A LIVE/DEAD™ BacLight™ bacterial viability kit (L13152) was purchased from the Invitrogen company.

### Synthesis of Ag@SnS<sub>2</sub> nanocomposites

First, SnS<sub>2</sub> was synthesized by a one-step hydrothermal method.<sup>42</sup> SnCl<sub>4</sub>·5H<sub>2</sub>O (1 mmol) and L-cysteine (5 mmol) were respectively dissolved in 30 mL of deionized (DI) water, and then they were put in the hydrothermal reactor and heated at 180 °C for 24 h in an oven. The products were centrifuged and washed with DI water and ethanol three times. A dark yellow SnS<sub>2</sub> powder was obtained by oven drying at 60 °C. Then Ag@SnS<sub>2</sub> was obtained by adding [Ag(NH<sub>3</sub>)<sub>2</sub>]<sup>+</sup> and H<sub>2</sub>O<sub>2</sub>. Briefly, AgNO<sub>3</sub> (2 mmol) was dissolved in 40 mL of DI water, and NH<sub>4</sub>OH was added dropwise to make an [Ag(NH<sub>3</sub>)<sub>2</sub>]<sup>+</sup> solution. Then a mixture of 26.9 mL of the [Ag(NH<sub>3</sub>)<sub>2</sub>]<sup>+</sup> solution and 0.1 mL of H<sub>2</sub>O<sub>2</sub> was added to a SnS<sub>2</sub> suspension (0.182 g SnS<sub>2</sub> dispersed in 40 mL of DI water), followed by stirring for 24 h with the color changing from dark yellow to black. Finally, Ag-functionalized SnS<sub>2</sub> nanocomposites were washed and dried for further use.

### Characterization

Microscopy images were obtained using a Transmission Electron Microscope (TEM) of JEOL JEM-1200EX. High-resolution TEM (HRTEM) characterization was performed using a JEOL JEM-1200EX. The surface morphologies of the Ag@SnS<sub>2</sub> materials and bacteria were observed using a Scanning Electron Microscope (SEM) of JSM-6700F. Element composition and mapping were analyzed by Energy Dispersive Spectroscopy (EDS). The UV/Vis absorption spectra were obtained using a Shimadzu UV-1800 spectrophotometer. The crystalline phase of the synthesized materials was studied by X-ray diffraction (XRD) using a Rigaku D-Max 2500 diffractometer. The oxidation states of elements were recorded using an X-ray photoelectron spectroscopy (XPS) spectrum. Fluorescence images of bacteria were obtained by fluorescence microscopy using an Olympus IX53.

### Photothermal performance

500 μL of the nanomaterial suspension at a certain concentration was irradiated with 808 nm laser at 1.9 W cm<sup>-2</sup> and the temperature was monitored for 5 min. The infrared thermal images of Ag@SnS<sub>2</sub> at various concentrations with irradiation for 5 min were recorded every minute using a Fluke Ti10 Infrared Camera. For the photo-stability test, Ag@SnS<sub>2</sub> dispersions were irradiated for 5 min and then cooled down naturally, and the laser was switched on and off 5 times. The photothermal conversion efficiency ( $\eta$ ) of Ag@SnS<sub>2</sub> was studied by Roper's method.<sup>43</sup>

### *In vitro* photothermal antibacterial assay

*E. coli* and *S. aureus* were used as model bacteria to study the *in vitro* photothermal bactericidal effects of Ag@SnS<sub>2</sub> by the plate counting method. The bacteria were incubated in LB broth medium for 12 h at 37 °C with stirring, and then the

bacteria were dispersed in PBS. 250  $\mu\text{L}$  of the  $\text{Ag@SnS}_2$  suspension in PBS (2.0, 1, 0.5, and 0.3  $\text{mg mL}^{-1}$ ) was added to 250  $\mu\text{L}$  of the bacterial solution at  $2.0 \times 10^6$  CFU  $\text{mL}^{-1}$ . The mixture was illuminated using an 808 nm laser for 0, 5, 10, 20, and 30 min, respectively. As a control, 250  $\mu\text{L}$  of  $\text{SnS}_2$  solutions at 0.5  $\text{mg mL}^{-1}$  was mixed with 250  $\mu\text{L}$  of the bacterial solution and then illuminated for 20 min. After equal incubation time, the treated bacteria were transferred to the agar plates and cultured at 37  $^\circ\text{C}$  for 24 h. The bacterial colonies were imaged and counted. The bacterial cell viability was calculated using untreated cells as the control.

### Fluorescence microscopic imaging of bacteria

Fluorescence microscopic imaging was used to distinguish between live and dead cells stained with a live/dead viability kit. 250  $\mu\text{L}$  of the bacterial solution ( $2.0 \times 10^8$  CFU  $\text{mL}^{-1}$ ) was added to 250  $\mu\text{L}$  of PBS or  $\text{Ag@SnS}_2$  (0.5  $\text{mg mL}^{-1}$ ) with or without NIR irradiation (1.9  $\text{W cm}^{-2}$ , 20 min). The treated bacterial cells were incubated with SYTO 9 and propidium iodide (PI) in the dark for 10 min. After staining, the free dye was removed by centrifugation and the cell precipitate was placed on the slides for imaging under a fluorescence microscope.

### SEM observation of bacteria

The *in vitro* antibacterial mechanism was observed by SEM. 250  $\mu\text{L}$  of the bacterial solution ( $2.0 \times 10^8$  CFU  $\text{mL}^{-1}$ ) in PBS was added to 250  $\mu\text{L}$  of PBS or  $\text{Ag@SnS}_2$  (0.5  $\text{mg mL}^{-1}$ ) with or without NIR irradiation (1.9  $\text{W cm}^{-2}$ , 20 min). The treated bacteria were fixed with 2.5% (v/v) glutaraldehyde and then dehydrated with gradient alcohol in turn. After centrifugation and washing, the concentrated bacteria were dripped onto the silicon chip and observed by SEM.

### *In vivo* mice wound disinfection

6–8 weeks old female BALB/c mice were obtained from the experimental animal center of Bethune Medical College (Changchun, China). An abscess on each mouse model was created by injection of 100  $\mu\text{L}$  of *S. aureus* bacteria at  $10^9$  CFU  $\text{mL}^{-1}$  under the epidermis and cultured for 1 day. The infected mice were randomly divided into four groups with three mice in one group. Then, 50  $\mu\text{L}$  of PBS or  $\text{Ag@SnS}_2$  (1.0  $\text{mg mL}^{-1}$ ) was injected into the infected abscess with or without NIR irradiation (0.9  $\text{W cm}^{-2}$  for 10 min). A thermal imaging camera recorded photos of treated mice. For 2 weeks, the size of the abscess and mouse weight were measured every day. At the end of the test, the epidermal tissue of abscesses and major organs of treated mice were collected and detected by H&E staining.

## Results and discussion

### Structure and morphology of $\text{Ag@SnS}_2$

$\text{SnS}_2$  was prepared by a one-step hydrothermal method, where  $\text{SnCl}_4 \cdot 5\text{H}_2\text{O}$  was the Sn source and L-cysteine was the S source.

$\text{SnS}_2$  exhibited a three-dimensional flower-like structure with a size of  $\sim 500$  nm in width, which was assembled by numerous thin nanosheets (Fig. S1†). Ag nanoparticles were then decorated on the surface of  $\text{SnS}_2$  to form  $\text{Ag@SnS}_2$  due to the affinity of Ag and SH on the surface of  $\text{SnS}_2$ . In comparison with  $\text{SnS}_2$ , the morphology of  $\text{Ag@SnS}_2$  did not show obvious changes and maintained a flower-like structure (Fig. 1a and b). HRTEM images of  $\text{Ag@SnS}_2$  showed that the lattice spacing distances of 0.28 nm and 0.24 nm belong to the (101) plane of  $\text{SnS}_2$  and (200) plane of Ag, respectively (Fig. 1c). The decorated Ag nanoparticles were visualized under HRTEM and their size was  $\sim 5$  nm (Fig. S2†). EDS results also showed that elements Ag, S, and Sn were the main components of  $\text{Ag@SnS}_2$  and Ag was distributed evenly on the surface of  $\text{Ag@SnS}_2$  (Fig. S3†). Additionally, the successful decoration of Ag was also confirmed by XRD. The sharp diffraction peaks of  $\text{SnS}_2$  can be indexed to the (001), (100), (101), (102), (110), (111), and (201) planes, and other sets of diffraction peaks were assigned to the (111), (200), (220) and (311) crystal planes of cubic Ag (Fig. 1d). No other peaks were detected, which confirms the phase purity.

XPS studies were performed to study the chemical state and elemental distribution. The elements of Ag, Sn, and S can be found in the XPS spectrum of  $\text{Ag@SnS}_2$  as shown in Fig. 2a–d. The peaks located near 368.0 eV and 374.0 eV could be assigned to Ag 3d<sub>5/2</sub> and Ag 3d<sub>3/2</sub> respectively with the energy difference of 6.0 eV, which is characteristic of Ag (Fig. 2a).<sup>44,45</sup> Two peaks of 486.7 eV and 495.1 eV correspond to two spin orbits of Sn 3d<sub>5/2</sub> and Sn 3d<sub>3/2</sub>, respectively, which confirmed the presence of Sn<sup>4+</sup> (Fig. 2b).<sup>46,47</sup> The XPS spectrum of S 2p is shown in Fig. 2c, where the two orbits (S 2p<sub>3/2</sub> and S 2p<sub>1/2</sub>) corresponding to the S<sup>2-</sup> in  $\text{SnS}_2$  appeared at 161.3 eV and 162.6 eV. These results further proved the successful synthesis of  $\text{Ag@SnS}_2$ .

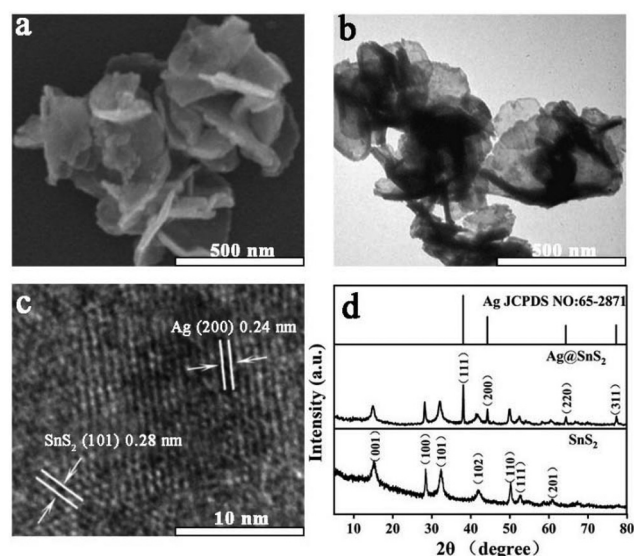


**Fig. 1** (a) SEM, (b) TEM, and (c) HRTEM images of  $\text{Ag@SnS}_2$ . (d) XRD patterns of  $\text{SnS}_2$  and  $\text{Ag@SnS}_2$ .



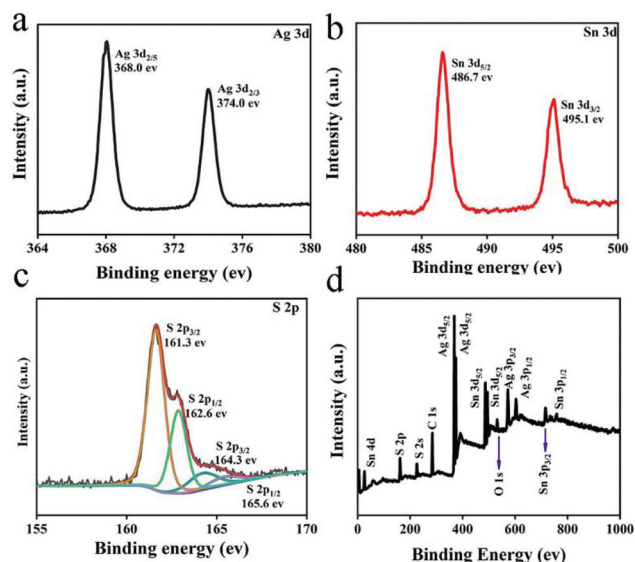


Fig. 2 XPS spectra of Ag@SnS<sub>2</sub>: (a) Ag 3d, (b) Sn 3d, (c) S 2P and (d) survey spectrum.

### Photothermal effect of Ag@SnS<sub>2</sub>

UV/Vis spectroscopy was applied to examine the optical behavior of Ag@SnS<sub>2</sub> and SnS<sub>2</sub>. As shown in Fig. 3a, SnS<sub>2</sub> showed a broad absorption range of 400–800 nm, while Ag@SnS<sub>2</sub> showed obviously enhanced absorption intensity with a red

shift due to the LSPR of Ag, especially the high NIR absorption. The results were favorable for the NIR-responsive photothermal conversion effect. The photothermal performance of Ag@SnS<sub>2</sub> was evaluated and their temperature changes under 808 nm laser irradiation are presented in Fig. 3b–f. After 5 min of laser irradiation, the temperature raise of Ag@SnS<sub>2</sub> at 1 mg mL<sup>−1</sup> was 50.0 °C, while the SnS<sub>2</sub> solution could only increase 24.1 °C (Fig. 3b). The results suggested that the decoration of Ag on SnS<sub>2</sub> can extensively enhance their light-to-heat conversion due to the LSPR absorption of Ag. A similar phenomenon was found in the literature where Ag decorated CeVO<sub>4</sub> semiconductors exhibited improved visible and NIR light absorption and resulted in a good photothermal effect due to the LSPR properties of Ag nanoparticles.<sup>39</sup> Additionally, the temperature rise of Ag@SnS<sub>2</sub> with different feeding mass ratios of SnS<sub>2</sub> and Ag was investigated under 808 nm laser irradiation (Fig. S4†). In order to maximize their photothermal conversion capability, the optimal feeding mass ratio of 1:0.8 (SnS<sub>2</sub>:Ag) was chosen to synthesize Ag@SnS<sub>2</sub> for the following experiments.

Encouraged by the good photothermal activity of Ag@SnS<sub>2</sub>, the concentration and laser power density-dependent photothermal effects were investigated. As expected, the temperature of Ag@SnS<sub>2</sub> elevated with the increase of materials concentration or laser power density (Fig. 3c and S5†). The corresponding thermal images of Ag@SnS<sub>2</sub> with 5 min of 808 nm NIR irradiation were captured, which was consistent with the temperature increase curve (Fig. 3c and d). The photo-stability of Ag@SnS<sub>2</sub> was also evaluated, where the samples were irra-

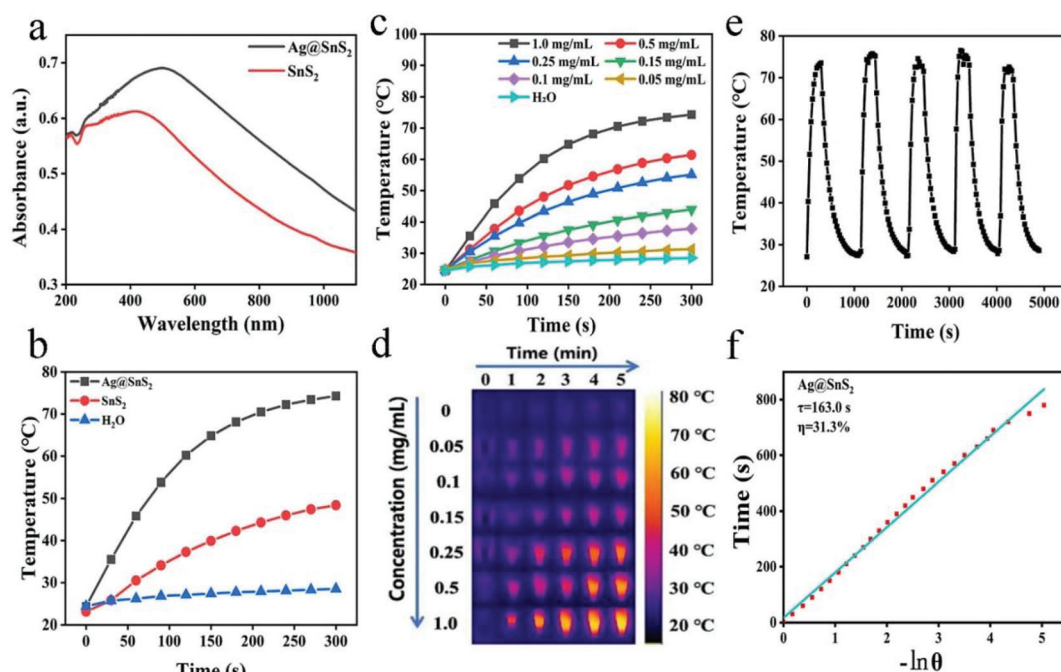


Fig. 3 (a) UV/Vis absorption of SnS<sub>2</sub> and Ag@SnS<sub>2</sub>. (b) Temperature profiles of SnS<sub>2</sub> and Ag@SnS<sub>2</sub> nanocomposites at 1 mg mL<sup>−1</sup> for 300 s via 808 nm laser irradiation. (c) Temperature profiles of Ag@SnS<sub>2</sub> with different concentrations and irradiation time. (d) The infrared thermal images of the Ag@SnS<sub>2</sub> aqueous solution at varying concentrations were taken before and after irradiation using an 808 nm laser. (e) Temperature changes of Ag@SnS<sub>2</sub> (1 mg mL<sup>−1</sup>) over five cycles using the 808 nm laser. (f) Linear regression curve of the cooling part from Ag@SnS<sub>2</sub>.

diated for 5 min and then cooled down naturally. As shown in Fig. 3e, no appreciable continuous reduction of temperature raise can be found after five cycles of laser switch on and off, indicating that the Ag@SnS<sub>2</sub> samples had excellent photothermal stability. The linear regression curve of Ag@SnS<sub>2</sub> (Fig. 3f) was obtained from cooling curves (Fig. S6†) according to Roper's report. The photothermal conversion efficiency ( $\eta$ ) and the time constant for heat transfer ( $\tau$ ) of Ag@SnS<sub>2</sub> were calculated to be 31.3% and 163.0 s, respectively.

### *In vitro* antibacterial effect of Ag@SnS<sub>2</sub>

To investigate the photothermal effect of Ag@SnS<sub>2</sub> against *E. coli* and *S. aureus*, bacteria were treated with different concentrations of Ag@SnS<sub>2</sub> (0–1.0 mg mL<sup>−1</sup>) at different laser irradiation times (0–30 min) and then cultured in agar plates at 37 °C. After 24 h of incubation, bacterial colonies grown on the agar plates were imaged and counted (Fig. 4). It was obvious that the bacterial viability decreased along with the increase of sample dosage and laser irradiation time. At 1.0 mg mL<sup>−1</sup> and 0.5 mg mL<sup>−1</sup> of Ag@SnS<sub>2</sub>, a 100% killing rate of both *E. coli* and *S. aureus* was observed when irradiated using an 808 nm laser for 5 min. At 0.25 mg mL<sup>−1</sup>, the killing rate can reach 99.2% for *E. coli* and 98.8% for *S. aureus* after 30 min of irradiation. When the concentration was further reduced to 0.15 mg mL<sup>−1</sup>, the killing rate was 76.9% for *E. coli* and 91.6% for *S. aureus* even after 30 min of irradiation. The results indicated that antibacterial agents at relatively low concentrations required a longer irradiation time to maintain almost complete inactivation of bacterial growth. The antibacterial effect of the SnS<sub>2</sub> control group was also analyzed using the plate counting method. We found that neither SnS<sub>2</sub> with NIR irradiation nor SnS<sub>2</sub> without NIR irradiation have antibacterial activities (Fig. S7†). Based on the results, a suitable dosage of Ag@SnS<sub>2</sub> and an irradiation time could be selected to achieve the suitable bacterial killing rate. Additionally, there

was no obvious death for Ag@SnS<sub>2</sub> treated bacterial cells without NIR irradiation, suggesting that the bactericidal activity of Ag@SnS<sub>2</sub> was not from their inherent chemical toxicity. The release of Ag from Ag@SnS<sub>2</sub> (1 mg mL<sup>−1</sup>) after NIR irradiation for 30 min was 0.49 µg mL<sup>−1</sup> analyzed by ICP-MS. The concentration of released Ag was too low to inhibit the bacterial growth, also demonstrating that the released Ag has a negligible antibacterial activity. The decoration of Ag nanoparticles mainly enhanced the photothermal effect of SnS<sub>2</sub>, but not the chemical toxicity. The inhibition of bacteria resulted from the NIR-induced hyperthermia from Ag@SnS<sub>2</sub>. Furthermore, hemolysis results showed that Ag@SnS<sub>2</sub> shows negligible hemolysis of red blood cells (RBCs) even at 1 mg mL<sup>−1</sup> (Fig. S8†), indicating the safety and practicability of the samples for further study *in vivo*.

We further investigated the *in vitro* photothermal antibacterial effect of Ag@SnS<sub>2</sub> using a fluorescent microscope. Based on the previous results, 0.25 mg mL<sup>−1</sup> of Ag@SnS<sub>2</sub> and 20 min of NIR irradiation time were chosen for the following experiments. After treatment, both *E. coli* and *S. aureus* bacteria were stained using a live/dead BacLight assay kit, where SYTO-9 stained the live bacteria (green fluorescence) and PI stained the dead bacteria (red fluorescence). As shown in Fig. 5, bacterial cells treated with Ag@SnS<sub>2</sub> under NIR irradiation exhibited a lot of red spots, while bacterial cells treated with PBS, NIR, and Ag@SnS<sub>2</sub> showed a lot of green spots and only a few red spots. The results were in agreement with the bacterial cell viability results, which further confirmed the photothermal antibacterial effects of Ag@SnS<sub>2</sub>.

To better assess the photothermal antibacterial effect, the morphology of *E. coli* and *S. aureus* exposed to Ag@SnS<sub>2</sub> plus 808 nm laser irradiation was investigated by SEM. When treated with PBS or NIR, *E. coli* cells were rod-shaped with the intact cell membrane (Fig. 6a and b), and similarly, *S. aureus* cells were sphere-shaped with a smooth surface (Fig. 6e and f). When incubated with Ag@SnS<sub>2</sub> without NIR irradiation, bacterial cells had obvious interaction with nanocomposites, and their cell membrane still maintained integrity, suggesting that Ag@SnS<sub>2</sub> alone had barely bactericidal activity (Fig. 6c and g). However, when exposed to Ag@SnS<sub>2</sub> plus NIR irradiation, the bacterial cells were collapsed obviously, indicating that NIR-induced hyperthermia can violently destroy the bacteria (Fig. 6d and h). It can be concluded that Ag@SnS<sub>2</sub> as a photothermal agent induced intensive antibacterial effect on the *E. coli* and *S. aureus* cells by the damage of cell membrane integrity.

### *In vivo* wound disinfection

Inspired by the excellent *in vitro* antibacterial effect of Ag@SnS<sub>2</sub>, their PTT-induced *in vivo* wound disinfection was further investigated. *S. aureus* is one of the leading pathogens responsible for healthcare-associated infection, and thus a mouse model was established by injecting *S. aureus* under its epidermis tissues to create the abscess infection. After 1 day, PBS or Ag@SnS<sub>2</sub> solution was injected into the infected abscess and the wound healing was monitored for 14 days. As

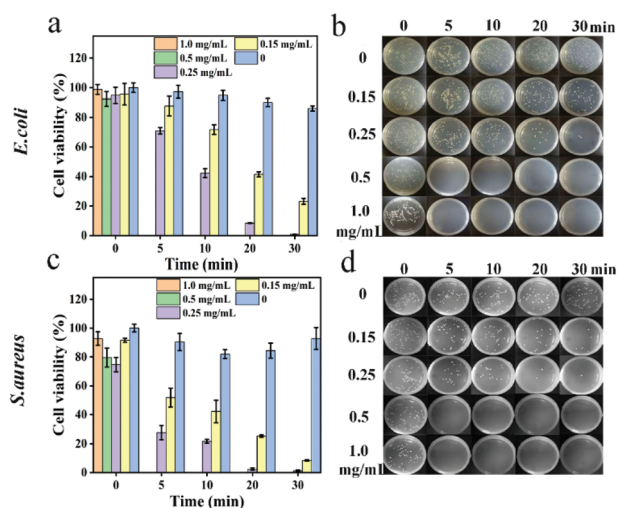


Fig. 4 (a and c) The cell viability and (b and d) photographs of bacterial colonies of (a and b) *E. coli* and (c and d) *S. aureus* exposed to Ag@SnS<sub>2</sub> (0–1.0 mg mL<sup>−1</sup>) at different times (0–30 min) of NIR irradiation.



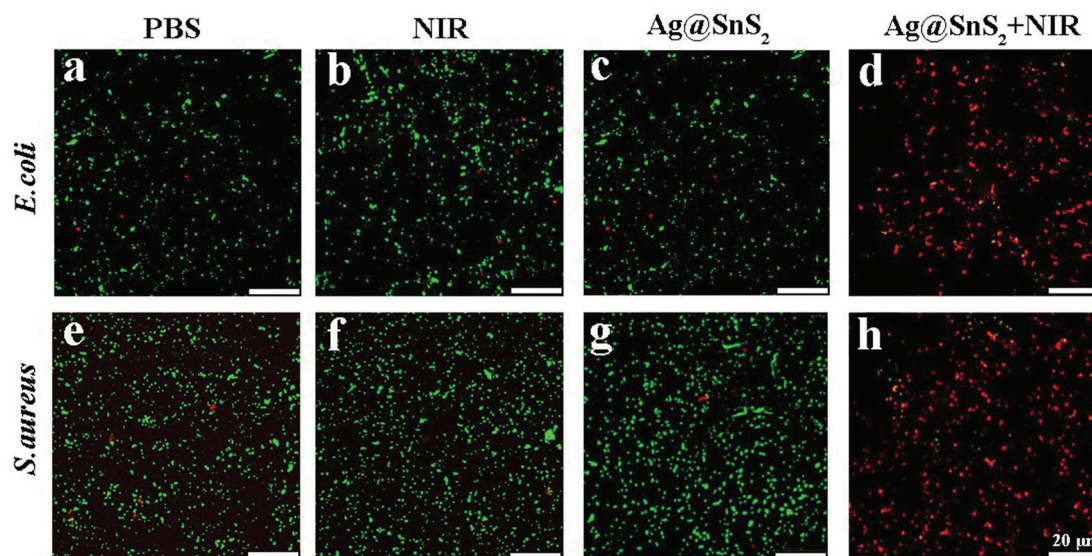


Fig. 5 Fluorescence microscopic images of (a–d) *E. coli* and (e–h) *S. aureus* treated with (a and e) PBS, (b and f) NIR irradiation, (c and g) Ag@SnS<sub>2</sub>, and (d and h) Ag@SnS<sub>2</sub> plus NIR irradiation and stained by SYTO 9 (green) and PI (red).

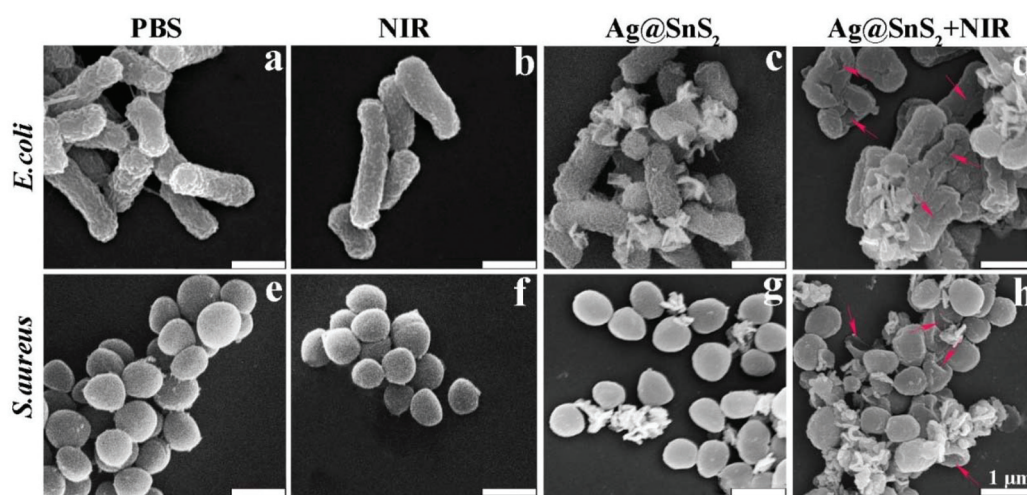


Fig. 6 SEM of (a–d) *E. coli* and (e–h) *S. aureus* treated with (a and e) PBS, (b and f) NIR irradiation, (c and g) Ag@SnS<sub>2</sub>, and (d and h) Ag@SnS<sub>2</sub> plus NIR irradiation. The red arrows indicate the damage of bacterial cells.

shown in Fig. 7a, an obvious swelling with a certain degree of redness developed after 1 day of bacterial infection. For PBS, NIR, and Ag@SnS<sub>2</sub> control groups, an obvious subepidermal abscess formed at the first few days, and then a local ulcer progressively formed from the abscess. At the end of 14 days, the red scar protruded after the wound healing and the surrounding skin was red and swollen. By contrast, the wound treated with Ag@SnS<sub>2</sub> plus NIR irradiation group healed much more quickly than that of control groups without the formation of obvious ulcers and scars. The sizes of abscesses or wound in the Ag@SnS<sub>2</sub> with NIR group were clearly less than those in control groups (Fig. 7b). During 10 min of NIR irradiation, the Ag@SnS<sub>2</sub> plus NIR group exhibited excellent

photothermal conversion efficiency and the temperature increased to 50.5 °C rapidly, while the temperature of the NIR group only reached 43.4 °C (Fig. 7c). The results indicated that Ag@SnS<sub>2</sub> with 808 nm laser irradiation underwent strong *in vivo* light-to-heat conversion, and the resulting hyperthermia successfully exerted wound disinfection. In addition, the mice bearing bacterial infection after various treatments exhibited no obvious bodyweight drop, which suggested the good biocompatibility of Ag@SnS<sub>2</sub> (Fig. 7d).

To further demonstrate the therapeutic status at the tissue level, the epidermal tissue was isolated and histologically analyzed at the end of 2 weeks. Regenerating epidermis in the Ag@SnS<sub>2</sub> with NIR group completely covered the wound, while

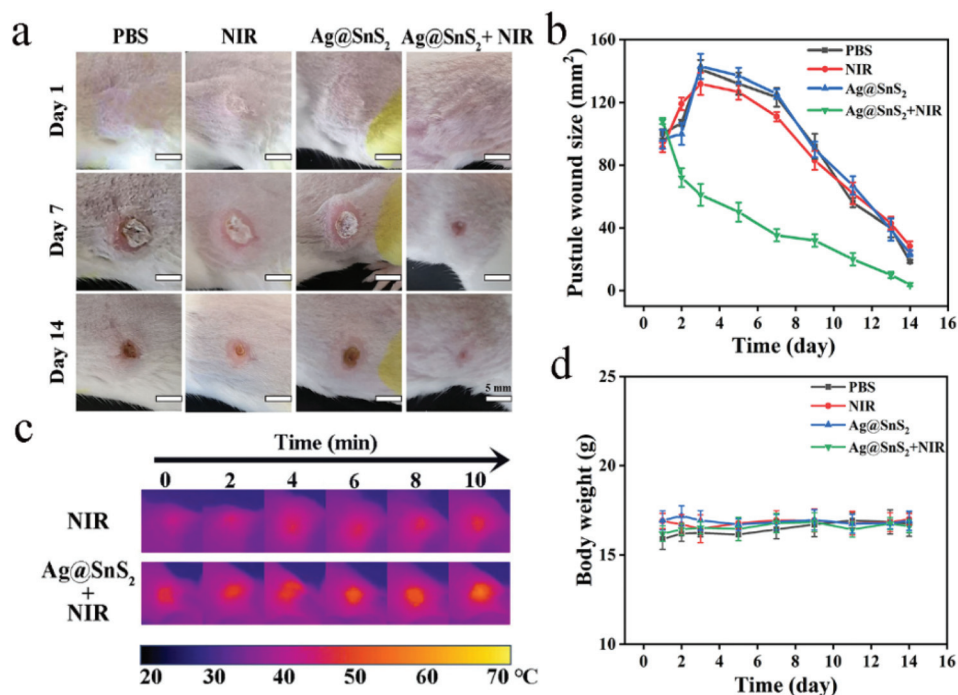


Fig. 7 (a) Photographs of *S. aureus* infected abscess and wound on mice with different treatments including PBS, NIR irradiation, Ag@SnS<sub>2</sub>, and Ag@SnS<sub>2</sub> plus NIR irradiation. (b) Graphical representation of the quantitative measurement of the wound area for 14 days. (c) Photographs and infrared thermal images of the wound area irradiated with an NIR laser for 0, 2, 4, 6, 8, and 10 min and (d) changes in the weight of mice for 14 days.

the epithelial regeneration was delayed in the other three groups (Fig. 8a). These demonstrated that Ag@SnS<sub>2</sub> could effectively prevent the bacterial infection *via* PTT under NIR irradiation and further accelerate the wound healing in the mouse model. In addition, the organs of mice treated with

Ag@SnS<sub>2</sub> alone and Ag@SnS<sub>2</sub> plus NIR were studied by H&E staining to analyze *in vivo* biocompatibility of Ag@SnS<sub>2</sub>. Fig. 8b shows no obvious difference with normal organs, demonstrating that Ag@SnS<sub>2</sub> has low cytotoxicity and good biocompatibility.

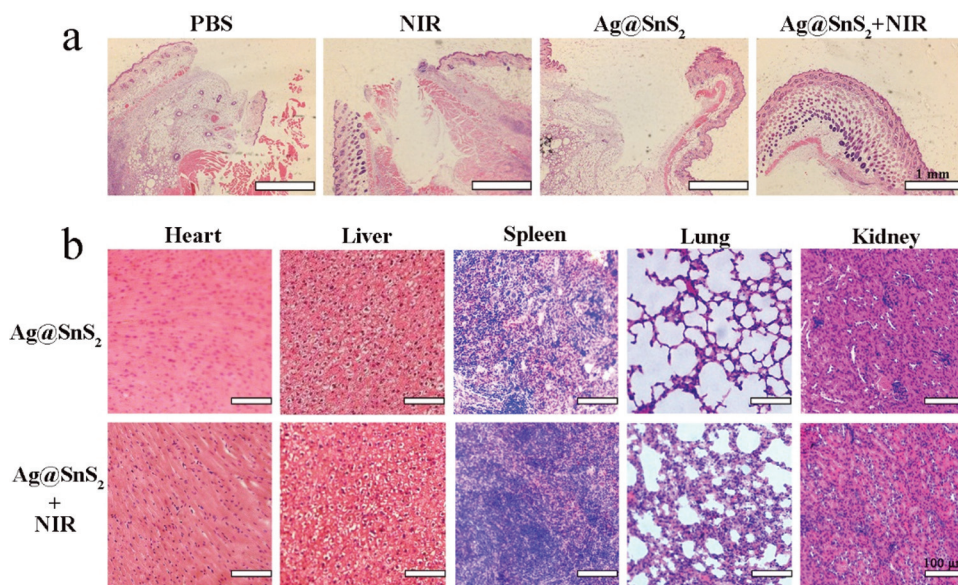


Fig. 8 (a) H&E staining of wound tissues treated with PBS, NIR irradiation, Ag@SnS<sub>2</sub>, and Ag@SnS<sub>2</sub> plus NIR irradiation after 14 days. (b) H&E staining of visceral organ sections treated with Ag@SnS<sub>2</sub> and Ag@SnS<sub>2</sub> plus NIR irradiation after 14 days.



## Conclusion

In summary, we established an excellent bactericidal nanocomposite based on novel metals integrated semiconductors. The decoration of Ag on SnS<sub>2</sub> maximized the LSPR of SnS<sub>2</sub> in the NIR window, improving their photothermal conversion capability. We demonstrated that Ag@SnS<sub>2</sub> exhibited a robust *in vitro* bactericidal activity, where both *E. coli* and *S. aureus* can be completely killed by Ag@SnS<sub>2</sub> under 808 nm laser irradiation. Furthermore, the *in vivo* wound disinfection tests in bacteria-infected mice proved that Ag@SnS<sub>2</sub> can efficiently cure the bacterial infection and expedite wound healing with the assistance of NIR irradiation. Therefore, the semiconductor/metal heterostructures have potential antibacterial applications, particularly suitable for clinical wound healing treatments.

## Author contributions

All authors approved the final version of the manuscript.

## Conflicts of interest

There are no conflicts of financial interest to declare.

## Acknowledgements

This work was supported by grants from the National Natural Science Foundation of China (Grant No. 51602123) and the National Key Research and Development Program of China (2018YFC1602504). All animal procedures were performed in accordance with the Guidelines for Care and Use of Laboratory Animals of SCXK (Jilin, China) with certificate no. 2016-0001 and approved by the Animal Ethics Committee of Jilin University.

## References

- 1 A. L. Hook, C. Y. Chang, J. Yang, S. Atkinson, R. Langer, D. G. Anderson, M. C. Davies, P. Williams and M. R. Alexander, *Adv. Mater.*, 2013, **25**, 2542–2547.
- 2 J. Huang, J. Zhou, J. Zhuang, H. Gao, D. Huang, L. Wang, W. Wu, Q. Li, D.-P. Yang and M.-Y. Han, *ACS Appl. Mater. Interfaces*, 2017, **9**, 36606–36614.
- 3 D. Hu, H. Li, B. Wang, Z. Ye, W. Lei, F. Jia, Q. Jin, K.-F. Ren and J. Ji, *ACS Nano*, 2017, **11**, 9330–9339.
- 4 Y. Xu, X. Liu, Y. Zheng, C. Li, K. W. K. Yeung, Z. Cui, Y. Liang, Z. Li, S. Zhu and S. Wu, *Bioact. Mater.*, 2021, **6**, 1575–1587.
- 5 S. K. Chaudhuri, S. Chandel and L. Malodia, *Nano Biomed. Eng.*, 2016, **8**, 1–8.
- 6 X. Yuan, M. I. Setyawati, D. T. Leong and J. Xie, *Nano Res.*, 2014, **7**, 301–307.
- 7 C. Wang, J. Li, X. Liu, Z. Cui, D.-F. Chen, Z. Li, Y. Liang, S. Zhu and S. Wu, *Biomater. Sci.*, 2020, **8**, 4216–4224.
- 8 Y. Xiang, Q. Zhou, Z. Li, Z. Cui, X. Liu, Y. Liang, S. Zhu, Y. Zheng, K. W. K. Yeung and S. Wu, *J. Mater. Sci. Technol.*, 2020, **57**, 1–11.
- 9 X. Zhang, G. Li, D. Wu, X. Li, N. Hu, J. Chen, G. Chen and Y. Wu, *Biosens. Bioelectron.*, 2019, **137**, 178–198.
- 10 X. Teng, X. Liu, Z. Cui, Y. Zheng, D.-f. Chen, Z. Li, Y. Liang, S. Zhu and S. Wu, *Prog. Nat. Sci.*, 2020, **30**, 677–685.
- 11 Y. Xu, J. Ma, Y. Han, H. Xu, Y. Wang, D. Qi and W. Wang, *Chem. Eng. J.*, 2020, **384**, 123379.
- 12 Q. Wu, X. Liu, B. Li, L. Tan, Y. Han, Z. Li, Y. Liang, Z. Cui, S. Zhu, S. Wu and Y. Zheng, *J. Mater. Sci.*, 2021, **67**, 70–79.
- 13 D. Han, Y. Han, J. Li, X. Liu, K. W. K. Yeung, Y. Zheng, Z. Cui, X. Yang, Y. Liang, Z. Li, S. Zhu, X. Yuan, X. Feng, C. Yang and S. Wu, *Appl. Catal., B*, 2020, **261**, 118248.
- 14 Y. Yang, Y. Deng, J. Huang, X. Fan, C. Cheng, C. Nie, L. Ma, W. Zhao and C. Zhao, *Adv. Funct. Mater.*, 2019, **29**, 1900143.
- 15 J. Nam, S. Son, L. J. Ochyl, R. Kuai, A. Schwendeman and J. J. Moon, *Nat. Commun.*, 2018, **9**, 1–13.
- 16 L. Zhao, W. Yuan, H. P. Tham, H. Chen, P. Xing, H. Xiang, X. Yao, X. Qiu, Y. Dai and L. Zhu, *Small*, 2017, **13**, 1700963.
- 17 S. Gai, G. Yang, P. Yang, F. He, J. Lin, D. Jin and B. Xing, *Nano Today*, 2018, **19**, 146–187.
- 18 J. Wang, D. Xu, T. Deng, Y. Li, L. Xue, T. Yan, D. Huang and D. Deng, *ACS Appl. Bio Mater.*, 2018, **1**, 1976–1984.
- 19 J. Li, J. Rao and K. Pu, *Biomaterials*, 2018, **155**, 217–235.
- 20 S. E. Skrabalak, J. Chen, L. Au, X. Lu, X. Li and Y. Xia, *Adv. Electron. Mater.*, 2007, **19**, 3177–3184.
- 21 H. Chen, L. Shao, T. Ming, Z. Sun, C. Zhao, B. Yang and J. Wang, *Small*, 2010, **6**, 2272–2280.
- 22 K. Yang, S. Zhang, G. Zhang, X. Sun, S.-T. Lee and Z. Liu, *Nano Lett.*, 2010, **10**, 3318–3323.
- 23 Y.-W. Chen, Y.-L. Su, S.-H. Hu and S.-Y. Chen, *Adv. Drug Delivery Rev.*, 2016, **105**, 190–204.
- 24 Y. Lin, D. Han, Y. Li, L. Tan, X. Liu, Z. Cui, X. Yang, Z. Li, Y. Liang and S. Zhu, *ACS Sustainable Chem. Eng.*, 2019, **7**, 14982–14990.
- 25 Q. Tian, M. Tang, Y. Sun, R. Zou, Z. Chen, M. Zhu, S. Yang, J. Wang, J. Wang and J. Hu, *Adv. Mater.*, 2011, **23**, 3542–3547.
- 26 Q. Yin, L. Tan, Q. Lang, X. Ke, L. Bai, K. Guo, R. Qiao and S. Bai, *Appl. Catal., B*, 2018, **224**, 671–680.
- 27 X. Huang, W. Zhang, G. Guan, G. Song, R. Zou and J. Hu, *Acc. Chem. Res.*, 2017, **50**, 2529–2538.
- 28 M. Sun, X. Zhao, Q. Zeng, T. Yan, P. Ji, T. Wu, D. Wei and B. Du, *Appl. Surf. Sci.*, 2017, **407**, 328–336.
- 29 A. Giberti, A. Gaiardo, B. Fabbri, S. Gherardi, V. Guidi, C. Malagù, P. Bellutti, G. Zonta, D. Casotti and G. Cruciani, *Sens. Actuators, B*, 2016, **223**, 827–833.
- 30 P. Sinsermsuksakul, R. Chakraborty, S. B. Kim, S. M. Heald, T. Buonassisi and R. G. Gordon, *Chem. Mater.*, 2012, **24**, 4556–4562.
- 31 R. S. Mane and C. D. Lokhande, *Mater. Chem. Phys.*, 2000, **65**, 1–31.



- 32 N. T. N. Truong and C. Park, *Electron. Mater. Lett.*, 2016, **12**, 308–314.
- 33 J. Hao, D. Zhang, Q. Sun, S. Zheng, J. Sun and Y. Wang, *Nanoscale*, 2018, **10**, 7210–7217.
- 34 Y. Zhang, F. Zhang, Z. Yang, H. Xue and D. D. Dionysiou, *J. Catal.*, 2016, **344**, 692–700.
- 35 D. Wang, M. Tang, H. Jiang, M. Li, S. Jiang, L. Sun and J. Sun, *Chem. Eng. J.*, 2020, **400**, 125814.
- 36 Z. Xiao, C. Xu, X. Jiang, W. Zhang, Y. Peng, R. Zou, X. Huang, Q. Liu, Z. Qin and J. Hu, *Nano Res.*, 2016, **9**, 1934–1947.
- 37 W.-N. Wang, P. Pei, Z.-Y. Chu, B.-J. Chen, H.-S. Qian, Z.-B. Zha, W. Zhou, T. Liu, M. Shao and H. Wang, *Chem. Eng. J.*, 2020, **397**, 125488.
- 38 Y. Cao, S. Li, C. Chen, D. Wang, T. Wu, H. Dong and X. Zhang, *Biomaterials*, 2018, **158**, 23–33.
- 39 M. Chang, M. Wang, Y. Chen, M. Shu, Y. Zhao, B. Ding, Z. Hou and J. Lin, *Nanoscale*, 2019, **11**, 10129–10136.
- 40 X. Ding, C. H. Liow, M. Zhang, R. Huang, C. Li, H. Shen, M. Liu, Y. Zou, N. Gao, Z. Zhang, Y. Li, Q. Wang, S. Li and J. Jiang, *J. Am. Chem. Soc.*, 2014, **136**, 15684–15693.
- 41 A. Agrawal, S. H. Cho, O. Zandi, S. Ghosh, R. W. Johns and D. J. Milliron, *Chem. Rev.*, 2018, **118**, 3121–3207.
- 42 I. Shown, S. Samireddi, Y.-C. Chang, R. Putikam, P.-H. Chang, A. Sabbah, F.-Y. Fu, W.-F. Chen, C.-I. Wu, T.-Y. Yu, P.-W. Chung, M. C. Lin, L.-C. Chen and K.-H. Chen, *Nat. Commun.*, 2018, **9**, 169.
- 43 D. K. Roper, W. Ahn and M. Hoepfner, *J. Phys. Chem. C*, 2007, **111**, 3636–3641.
- 44 Q. Xiang, J. Yu, B. Cheng and H. Ong, *Chem. – Asian J.*, 2010, **5**, 1466–1474.
- 45 J. Cao, B. Luo, H. Lin, B. Xu and S. Chen, *J. Hazard. Mater.*, 2012, **217**, 107–115.
- 46 X. Cui, W. Xu, Z. Xie and Y. Wang, *J. Mater. Chem.*, 2016, **4**, 1908–1914.
- 47 L. Shi, S. Liu and Z. He, *Appl. Surf. Sci.*, 2018, **457**, 1035–1043.